

Photoelectrochemical properties of plasma-induced nanostructured tungsten oxide

Shuangyuan FENG¹⁾, Shin KAJITA²⁾, Masanobu HIGASHI³⁾, Anja BIEBERLE-HÜTTER⁴⁾, Tomoko YOSHIDA³⁾, and Noriyasu OHNO¹⁾

¹⁾*Graduate School of Engineering, Nagoya University, Nagoya 464-8603, Japan*

²⁾*Institute of Materials and Systems for Sustainability, Nagoya University, Nagoya 464-8603, Japan*

³⁾*Advanced Research Institute for Natural Science and Technology, Osaka City University, Osaka 558-8585, Japan*

⁴⁾*Dutch Institute for Fundamental Energy Research (DIFFER), P.O. Box 6336, 5600 HH Eindhoven, The Netherlands*

March 16, 2022

Helium (He)-induced nanostructured tungsten sheets were synthesized by He plasma irradiation under different plasma exposure durations. After calcination, nanostructured tungsten oxide samples were used as photoelectrodes to test photoelectrochemical (PEC) performance. The results showed that nanostructured WO₃ photoanodes have higher PEC performance compared to the sample without nanostructures. The 15 min irradiated sample had the highest photocurrent density of 3.5 mA/cm² under the thermodynamic potential of water oxidation (1.23 V vs. RHE). It was found that the oxide layer thickness and exposed crystal facet have a significant impact on PEC performance. The plasma synthesis technique has proved to be an effective method for preparing nanostructured WO₃ photoelectrodes.

Keywords: Nanostructured tungsten, plasma irradiation, PEC water splitting, IPCE

author's e-mail: feng.shuangyuan@d.mbox.nagoya-u.ac.jp

1 Introduction

Owing to the exhaustion of non-renewable resources, such as fossil fuels, and the increasing severity of environmental pollution, the development and utilization of clean and renewable energy are extremely urgent. Among them, hydrogen energy is considered one of the ideal clean and renewable energies that can replace fossil fuels. The best choice for a sustainable, affordable, clean, and available form of energy is solar energy. Of the many methods for using solar energy, photoelectrochemical (PEC) water splitting has great development and utilization prospects due to its simple operation, low preparation cost, high efficiency, green and pollution-free nature, and other advantages [1–6]. The key component in the PEC system is the photoelectrode material. Tungsten trioxide (WO_3) is an emerging candidate with a suitable bandgap (2.5—2.9 eV [7–9]) and excellent chemical stability in acidic solutions [10, 11]. Nevertheless, the PEC performance of WO_3 remains low owing to its low solar spectrum utilization, slow charge transfer at WO_3 /electrolyte and serious electron-hole recombination [12, 13]. Semiconductor photoelectrode with complex nanostructure can improve not only the specific surface area but also the carrier transport and light trapping performance [14–16]. Surface nanostructuring, as one of the mainstream strategies for enhancing photocatalytic activity, has received considerable attention. Nanostructured WO_3 is often used as a photocatalyst due to its versatile advantages [17, 18].

Fiberform nanostructure (FN) has been found to form on the tungsten (W) surface by helium (He) plasma irradiation. Yajima and Kajita have found that FN materials show large surface areas and high optical absorptivity, respectively [19–21]. Because of these excellent characteristics, FN materials have the potential to enhance PEC performance. In addition, the plasma synthesis technique can offer significant advantages, such as high homogeneity, size-control ability, and easy manipulation [22].

To take full advantage of FN materials and plasma synthesis techniques, great efforts have been devoted to introducing FN to improve photocatalytic activity. Komori et al. reported that partially oxidized FN WO_3 is an excellent photocatalyst for the decolorization of methylene blue (MB) under near-infrared light ($\lambda > 800$ nm) [23]. Apart from W, molybdenum (Mo), iron (Fe), and other metal surfaces can also form FN during He plasma exposure [24, 25]. Respini et al. [26] showed that the performance of nanostructured WO_3 discs can be increased by plasma nanostructuring. Further research is now needed to look for high-performing photoelectrodes by plasma nanostructuring and then establish the relation between

PEC performance and the characterization of the photoelectrode. Bieberle-Hütter et al. [27] transferred this process to thin films and showed that nanostructures can be formed on typical PEC substrates (metal oxide photoelectrode on fluor-doped tin oxide on glass). The nanostructures adhere well to the substrate after oxidation. Sinha et al. [28] investigated the effect of these helium plasma-induced nanostructured iron-oxide thin films on the PEC water-splitting performance and found that short plasma-exposed thin films show the highest photocurrent. This plasma synthesis technique provides a possible preparative route for high performing WO_3 photoelectrodes. Efforts should be made to find the optimal conditions (irradiation time and calcination temperature) to obtain a high photocurrent electrode.

For this paper, nanostructured WO_3 photoelectrodes were synthesized from tungsten sheets by He plasma irradiation followed by calcination treatments and characterized by XRD (x-ray diffraction), XPS (x-ray photoelectron spectroscopy), SEM (scanning electron microscope), and Raman spectroscopy. The PEC cell system was used to evaluate the activity of nanostructured WO_3 photoelectrodes. The effects of helium ion fluence and calcination temperature on the PEC performance of nanostructured WO_3 photoelectrodes were investigated.

2 Experimental setup

2.1 Photoelectrode preparation

The samples used in this experiment are $10 \times 10 \text{ mm}^2$ tungsten sheet (Nilaco, 0.2-mm thickness, 99.95%). The samples were dipped into deionized water and ethanol and cleaned with an ultrasonic washer for 15 min. After cleaning and drying, the samples were irradiated with helium plasma to obtain surface nanostructuring using the linear plasma device NAGDIS-II, where high density helium plasma is formed by a direct current arc discharge using a LaB_6 cathode. The electron density and temperature were $\sim 10^{18} - 10^{19} \text{ m}^{-3}$ and $\sim 5 \text{ eV}$, respectively, measured with a single probe. By changing the helium flux and bias voltage of the W sample, the surface temperature and incident ion energy of the W sample were controlled. As shown in previous studies [29, 30], the thickness of the nanostructured layer is proportional to the square root of the helium ion fluence. To find the effects of the thickness of the nanostructured layer on the PEC activity, the tungsten sheet was irradiated by the helium plasma

for various exposure times (15, 30, 45 min) with a flux of $\sim 10^{22} \text{ m}^{-2}\text{s}^{-1}$. The nanostructured sheet without calcination is named A-W, where A represents the He plasma irradiation time in minutes as 0 min, 15 min, 30 min, and 45 min. To obtain the oxide, all nanostructured tungsten (W) and pristine W were oxidized at 673—973 K for 30 min using an electric furnace in air. Zhao et al. [31] found that the annealing atmosphere had no impact on the crystal structure and that WO_3 annealed in air had the highest photocurrent (compared to annealing in oxygen or nitrogen). Therefore, a calcination atmosphere in air was chosen for this study. The letter B in the general name A- WO_3 -B indicates the calcination temperature.

2.2 Characterizations

Cross-sectional SEM samples were prepared using pliers. The cross-sectional morphologies were investigated by an SEM (S4300, HITACHI) with the secondary electron detector and 15 kV accelerating voltage using a cross-section observation stage. The elemental analysis of the cross-section was performed by a JEOL JSM-6610A SEM with energy dispersive x-ray spectroscopy (EDS) integration. The crystalline phase was analyzed by a Rigaku ATX-G XRD with a $\text{Cu K}\alpha$ source in the $2\theta/\theta$ scanning mode for the 2θ range of 20 to 80 degrees. XPS measurements were performed using an ESCALAB 250Xi XPS device with an $\text{Al K}\alpha$ source. The Raman spectra of the samples were measured using an NRS-1000 laser Raman spectrophotometer in the range of 1155—50 cm^{-1} . The optical property of the samples was determined using a diffuse reflectance ultraviolet-visible (UV-Vis) spectrophotometer (Shimadzu UV-2600).

2.3 Photoelectrochemical measurements

PEC characterization was carried out using a potentiostat (BioLogical SP-150) under a standard three-electrode system. The prepared sample, a coiled Pt wire, and an $\text{Ag}/\text{AgCl}/\text{sat. KCl}$ electrode were used as the working electrode (WE), the counter electrode (CE), and the reference electrode (RE), respectively. The electrolyte was a 0.5 M sulfuric acid solution with a pH of 0.3. In the three-electrode system, the bias voltage applied between the WE and the RE was given versus the reversible hydrogen

electrode (RHE) by the following relation [31]:

$$\Phi_{\text{RHE}} = \Phi_{\text{Ag/AgCl}} + \Phi_{\text{Ag/AgCl}}^0 + 0.059 \times \text{pH} \quad (\Phi_{\text{Ag/AgCl}}^0 = +0.197\text{V}). \quad (1)$$

Illumination was provided by a 300 W Xe lamp. Linear sweep voltammetry (LSV) curves were collected at potentials between 1.5 V and 0.2 V versus Ag/AgCl electrode at a scan rate of 10 mV/s under chopped incident light with a controlled shutter at a rate of 0.5 s⁻¹.

The Xe lamp light source and monochromatic filters (Edmund optics) were used to emit monochromatic light of different wavelengths for the incident-photon-to-current conversion efficiency (IPCE) measurement. A power and energy meter (PM100USB, THORLABS) was used to record the intensity of monochromatic light (J_{light} , mW cm⁻²) at different wavelengths, and the IPCE value at different wavelengths was calculated from the following relation (2):

$$\text{IPCE}(\%) = \frac{J(\text{mA cm}^{-2}) \times 1239.8(\text{V nm})}{\lambda(\text{nm}) \times J_{\text{light}}(\text{mW cm}^{-2})} \times 100, \quad (2)$$

where λ is the wavelength of incident light, J is the photocurrent density, and J_{light} is the power density of monochromatic light.

3 Results and discussion

3.1 Helium plasma exposure time

3.1.1 Characterization

The effect of the irradiation time on the thickness of the nanostructure and PEC activity is explored while keeping other irradiation conditions and the calcination temperature of 773 K unchanged. The cross-sectional SEM images of the nanostructured sheet samples (15min-W, 30min-W, and 45min-W) can refer to Figure 2(b', d', and e') in reference [32]. The fluences of Figure 2(b', d', and e') in reference [32] are similar to that of 15min-W, 30min-W, and 45min-W. Figure 1(a, d, g) shows the sample cross-sectional SEM images of 15min-WO₃-773K, 30min-WO₃-773K, and 45min-WO₃-773K, respectively. It is seen that nanostructures are formed on the surface. The thickness increases from a few nanometers

to a few micrometers with increasing irradiation time. Figure 1 (b, e, h) and Figure 1(c, f, i) show EDS signal mappings of W and O, respectively. As can be seen from the SEM and EDS mappings, there is a clear boundary between the metal W layer and the top WO₃ layer, suggesting that the FN layer has already been fully oxidized at this temperature (773 K). With increasing irradiation time, the thickness of the oxidized layer increases. It is seen that the top part is oxidized at this calcination temperature, while the part below the boundary is metallic W. The top part consists of a nanostructured and bulk part. The oxidized thickness of the bulk part is comparable to or less than 1 μm. From Figure 1(b, e, h) and (c, f, i), it is difficult to provide any direct calcination thickness comparison between the nanostructured and bulk parts, so semi-quantitative calcination based on EDS signal mappings of W and O is performed later.

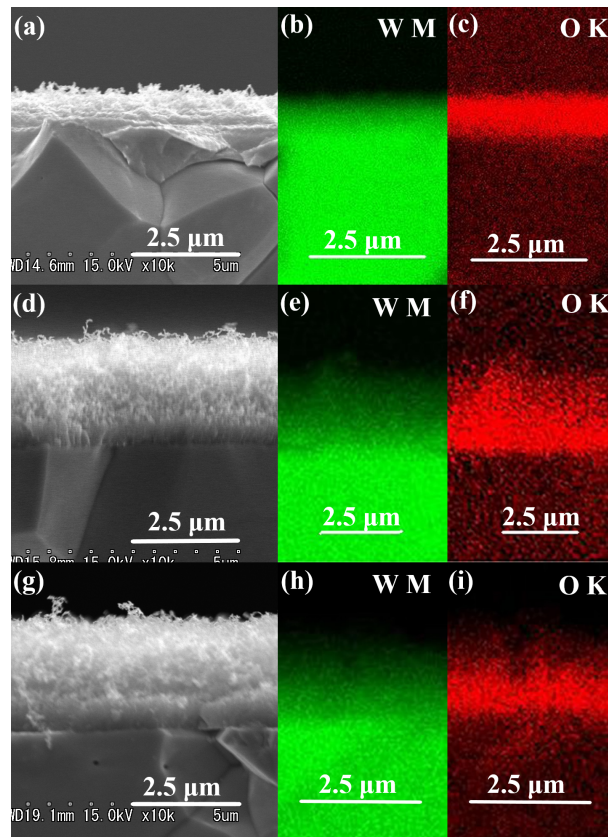


Fig. 1 Cross-section SEM images of (a) 15min-WO₃-773K, (d) 30min-WO₃-773K, (g) 45min-WO₃-773K; (b, e, h) and (c, f, i) are elemental maps of W and O, respectively.

Figure 2 shows x-ray diffraction (XRD, ATX-G) patterns of 0min-WO₃-773K, 15min-WO₃-773K, 30min-WO₃-773K, and 45min-WO₃-773K. The crystal structures of the samples are monoclinic WO₃

(JCPDS card no. 83-0950, $a=7.301 \text{ \AA}$, $b=7.539 \text{ \AA}$, $c=7.690 \text{ \AA}$, $\beta=90.892^\circ$). The diffraction peaks of the W metal substrate can be seen at $\theta=40.3^\circ$, 58.2° , and 73.2° , which correspond to the (110), (200), and (211) facets of cubic W, respectively [33, 34]. In addition to the diffraction peaks of W, the characteristic diffraction peaks at $2\theta=23.1^\circ$ and 23.6° and correspond to the (002) and (020) facets of monoclinic WO_3 , respectively. At the same calcination temperature, there is no difference in the crystal structure, even at different nanostructure layer thicknesses. Figure 3 shows XPS W4f spectra of pristine and nanostructured samples. No W peaks were detected on the surface, demonstrating that the surface was completely oxidized at 773 K. The O1s spectra for all the samples are provided in the supporting information. The O1s peak at the lowest binding energy (529.9 eV) corresponds to the lattice oxygen (O^{2-}), the peak at 530.5 eV is attributed to the surface oxidative oxygen O_2^-/O^- , and the third peak at the highest binding (531.5 eV) can be assigned to adsorbed O_2 [35, 36]. The UV-Vis diffuse reflectance spectra of 0min- WO_3 -773K, 15min- WO_3 -773K, 30min- WO_3 -773K, and 45min- WO_3 -773K were displayed in Figure S1-7(a). Details are provided in the supporting information.

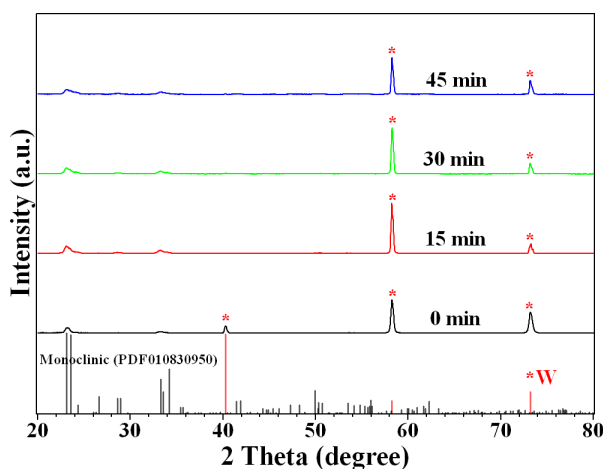


Fig. 2 XRD pattern of 0min- WO_3 -773K, 15min- WO_3 -773K, 30min- WO_3 -773K, 45min- WO_3 -773K.

3.1.2 Photoelectrochemical measurements

Figure 4 shows photocurrent density as a function of applied potential for 0min- WO_3 -773K, 15min- WO_3 -773K, 30min- WO_3 -773K, and 45min- WO_3 -773K under a chopped light source. The arrow in Figure 4 represents scanning from high to low potential. The 0min- WO_3 -773K photoelectrode shows the weakest photocurrent density of about 0.3 mA/cm^2 at 1.23 V vs. RHE (Figure 4, black curve).

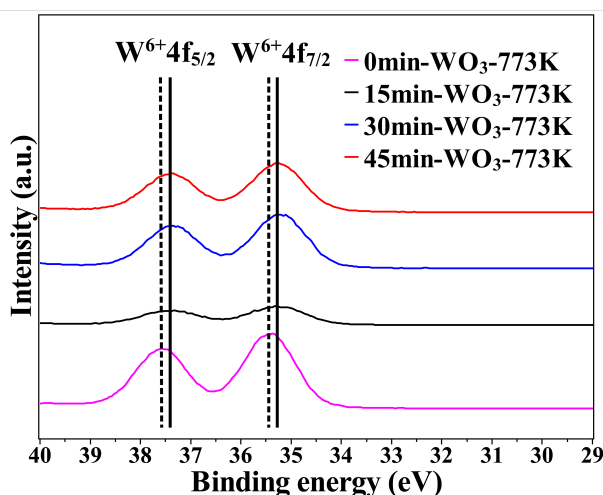


Fig. 3 XPS W4f spectra of 0min-WO₃-773K, 15min-WO₃-773K, 30min-WO₃-773K, 45min-WO₃-773K.

Respinis et al. have reported on polished tungsten after annealing at 700 °C for 1 h, showing a photocurrent density of about 0.2 mA/cm² at 1.23 V vs. RHE [26]. Zhao et al. have found for WO₃ thin films deposited by atomic layer deposition and annealed in air a photocurrent density of 0.1 mA/cm² at 1.23 V vs. RHE [31]. Here, the photocurrent density of the unexposed sample is slightly higher than the values from the literature [26, 31]. This may be because the W of the substrate makes it easier for electrons to be transported and because of the moderate thickness of the oxide layer at this calcination temperature. The sample with a plasma exposure time of 15 min exhibited the highest photocurrent density, reaching 3.5 mA/cm² at 1.23 V vs. RHE (Figure 4, red curve), which is 12 times higher than that of the 0min-WO₃-773K photoelectrode. The increase in photocurrent density is attributed to the formation of the nanostructure. The experiment was repeated three times using 15min-WO₃-773K photoelectrodes; results are shown in Figure S1-2 in the supporting information. The repeated experiment results show that the high photocurrent density can be achieved by the formation of the nanostructure. When the irradiation time increased from 15 to 30 min, the photocurrent density decreased, indicating that an appropriate oxide thickness is necessary. This is likely because a thin WO₃ layer of the 15 min irradiated sample makes it easier for electrons to move efficiently to the back. Due to diffusion and external bias, the photogenerated electrons can be quickly guided to the cathode, while the photogenerated holes remain on the surface of the photoanode material to participate in the oxidation reaction. This process thereby effectively inhibits the recombination of electron-hole pairs, thus greatly improving efficiency. Past research has shown that the surface oxidative oxygen (O₂²⁻/O⁻) is beneficial to improving

the PEC performance [36–38]. When the irradiation time continued to increase from 30 to 45 min, the photocurrent increased again. The increase is related to a higher $\text{O}_2^{2-}/\text{O}^-$ concentration (Table S1 and Figure S1-4), which outweighs the decrease due to increased thickness.

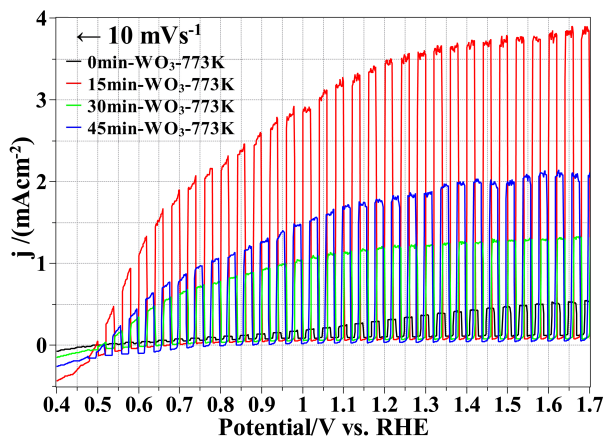


Fig. 4 Photocurrent density vs. applied potential curves of 0min-WO₃-773K, 15min-WO₃-773K, 30min-WO₃-773K, and 45min-WO₃-773K under chopped light.

3.2 Calcination temperature

3.2.1 Characterization

It was found that the calcination conditions (temperature, time) have a remarkable effect on the structure and activity of the photocatalysts [39]. Here, we investigate the calcination temperature dependence using the sample with the irradiation time of 15 min, which had the best performance at a calcination temperature of 773 K. In order to evaluate the thickness of the WO₃ layer at different calcination temperatures, the ratio of O to W was assessed based on the EDS elemental analysis. When 95% W is present and the remaining 5% is tungsten trioxide, the O/(O+W) (atom%) is about 13 (atom%). To measure the thickness of the WO₃ layer, we used the O atomic fraction, O/(O+W), of 13% as a threshold to distinguish the oxidized layer from bulk W. Figure 5(a) shows the depth profile of the oxygen atomic fraction of 15min-WO₃-773K. The oxide layer was roughly 2 μm thick. Figure 5(b) shows the oxide thickness as a function of the calcination temperature. The 15min-WO₃-673K sample is not shown, since the oxide layer was too thin to get the elemental diagrams of W and O clearly. It can be seen that the thickness of the oxide layer gradually increases with an increase in the calcination temperature.

Of all the samples, the oxide thickness of WO_3 -973K is the thickest and close to $25\ \mu\text{m}$. The oxide layer consists of a nanostructured and a bulk oxide layer. The dashed line value in Figure 5(b) is the thickness of the nanostructured layer (refer to Figure 1[a]). Figure 1(a) clearly shows the thickness of the nanostructured layer, which is about $0.5\ \mu\text{m}$. In order to determine the effect of different calcination temperatures on the surface structure, Raman spectra and XRD were subsequently performed.

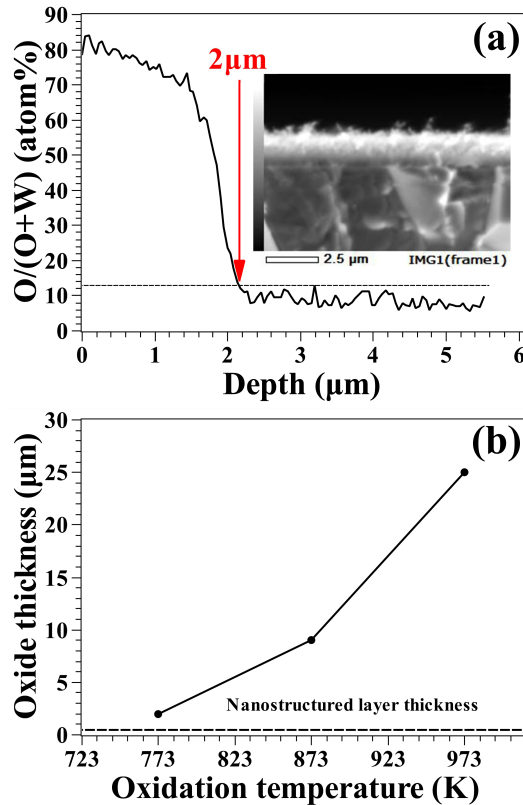


Fig. 5 a) Semi-quantitative calculation diagrams of oxidation rate with thickness from the EDS elemental analysis, inset view: Cross-section SEM images of 15min- WO_3 -773K; b) Diagram of oxide thickness with temperature. The dashed line is the thickness of the nanostructured layer.

The Raman spectra in the range of 1155 — $50\ \text{cm}^{-1}$ measured on the nanostructured samples annealed at 673 — $973\ \text{K}$ are shown in Figure 6. WO_3 vibrations have three main regions at 900 — 600 , 400 — 200 and below $200\ \text{cm}^{-1}$, which correspond to the stretching (ν), deformation (δ), and lattice modes, respectively [40]. Since the vibrational modes at low frequencies are associated with the lattice modes [41–43], the crystalline phase can be obtained by analyzing the low-frequency peaks (up to $200\ \text{cm}^{-1}$). The low-frequency peaks correspond to the lattice modes of librational nature and are affected by the low-symmetry phases of WO_3 [41–43]. The high-frequency peaks of 807 and $715\ \text{cm}^{-1}$ are also typ-

ical Raman peaks of the monoclinic phase, which correspond to the stretching vibrational modes [42]. The high- and low-frequency peaks indicate that the nanostructured WO_3 calcination at 673—973 K is in the monoclinic phase.

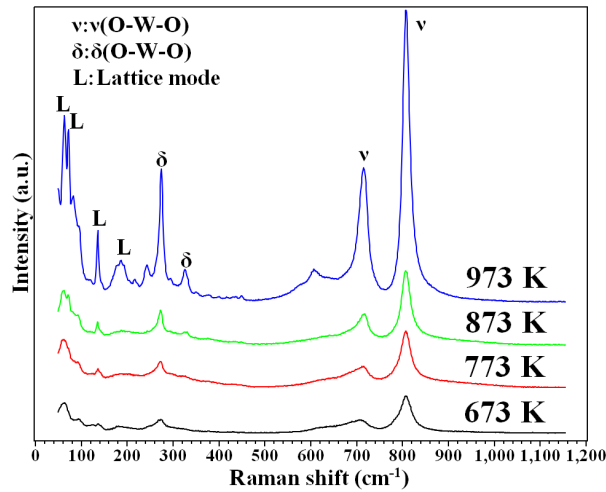


Fig. 6 Raman spectra of nanostructured WO_3 annealed at different temperatures.

Figure 7 provides XRD data obtained at different calcination temperatures. With the increase of the calcination temperature, the relative intensity of the (002) crystal facet is enhanced, indicating that the higher the temperature is, the more favourable it is for WO_3 to grow along the (002) crystal facet. The strongest peak of the (002) facet is observed for all the samples, apart from the sample calcined at 873 K. The sample calcined at 873 K prefers to grow along the (020) crystal facet. Figure S1-7(c) shows the UV-Vis diffuse reflectance spectra of 15min- WO_3 -673K, 15min- WO_3 -773K, 15min- WO_3 -873K, and 15min- WO_3 -973K. Details are also provided in the supporting information.

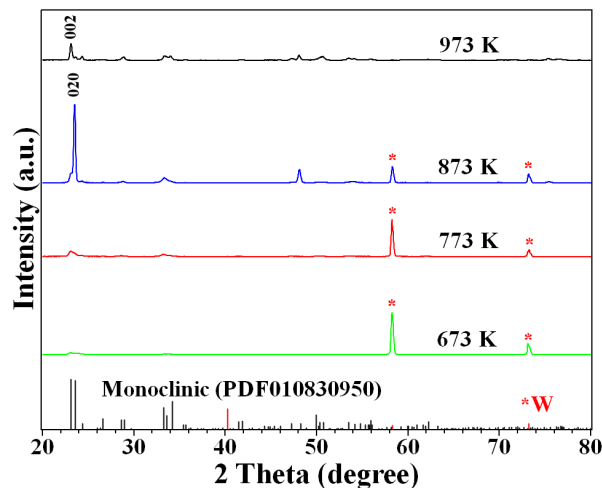


Fig. 7 XRD pattern of 15min- WO_3 -673K, 15min- WO_3 -773K, 15min- WO_3 -873K, and 15min- WO_3 -973K.

3.2.2 Photoelectrochemical measurements

In order to understand the changes in 15min-WO₃-X PEC performance, photocurrent tests on samples annealed at different temperatures were carried out, as shown in Figure 8. Among all the samples, the 15min-WO₃-773K electrode has the best photocurrent density of 3.5 mA/cm² at 1.23 V vs. RHE. Furthermore, a stability test of the 15min-WO₃-773K electrode was conducted for 1 h. Details are provided in the supporting information (Figure S1-1). One possible reason for the poor stability is the poor attachment of the nanostructured oxide layer on the W substrate, making it easy to remove [44]. Meanwhile, it was also found that after the PEC measurements, the thickness of the nanostructure was reduced, resulting in the photocurrent density getting worse. It has been suggested that the composite photocatalysts showed good stability [45]. It provides a new thought for exploring highly efficient and reusable photoelectrode materials.

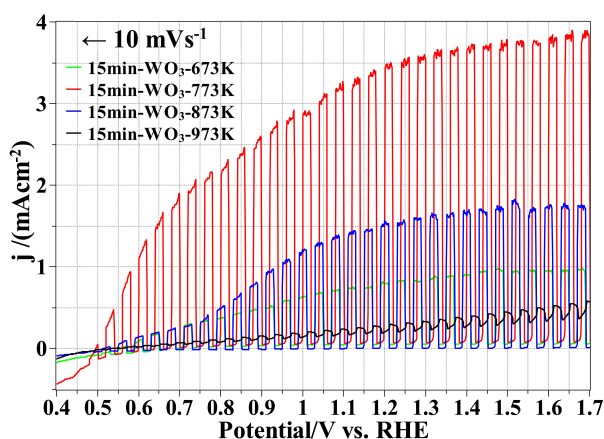


Fig. 8 Photocurrent density vs. applied potential curves of 15min-WO₃-673K, 15min-WO₃-773K, 15min-WO₃-873K, 15min-WO₃-973K under chopped light.

By analyzing the photocurrent densities, it was found that the photocurrent densities raised at first, then decreased, and the peak appeared at 15min-WO₃-773K. In this study, the photocatalytic activity was the highest when the oxide layer thickness was about 2 μ m. Appropriate oxide layer thickness is beneficial to the movement of photogenerated electron-hole pairs and improves photocatalytic activity, as has been discussed [46]. Also, it has been discussed that the fabrication of unique structures with specific exposed crystal facets provides an excellent platform for WO₃ PEC performance tuning [11]. The different facets exposed in photocatalysts significantly affect their surface properties [11, 47–49].

Gong et al. found that the larger surface energy of (002) facets than other facets contributes to improved PEC activity [50]. Wang et al. found that the (002) facet was more beneficial to the separation of electron-hole pairs [51] than the (200) facet.

Different crystal facets have surface energies following the order of (002)(1.56 J m⁻²)>(020)(1.54 J m⁻²)>(200)(1.43 J m⁻²) [52]. The photocurrent density of 15min-WO₃-873K at 1.23 V vs. RHE with exposed (020) facets is lower than that of 15-WO₃-773K with exposed (002) facets. The reason is the synergy between the slightly lower surface energy of the (020) facet and the thicker oxide thickness of 15min-WO₃-873K, while the oxide layer of 15min-WO₃-973K is too thick to obtain excellent PEC performance. Considering these analyses, the reason for the highest performance is likely the proper oxide thickness and more (002) facets, which are beneficial to the separation of electron-hole pairs, thus improving the PEC performance. From the calcination temperature dependence, the PEC properties of 15min-WO₃-X electrode materials are mainly affected by the thickness and crystal structure characteristics.

Figure 9 shows the wavelength dependence of the IPCE of the 15min-WO₃-773K sample. The sample has a strong light response between 300 and 450 nm, and the maximum efficiency reaches 53% at 355 nm. The efficiency decreases to almost zero when the wavelength is larger than 450 nm. The fabrication method, morphology, and crystallinity are the common factors affecting IPCE value [53]. The maximum IPCE value for nanoporous WO₃ photoanodes using the anodization method at 340 nm was approximately 92% [54]. The highest IPCE value in this study was 54% at 355 nm, which is 0.6 times the above data. The highest IPCE value at 370 nm was 22% in Respinis [26]. This shows that the highest IPCE is found at different wavelengths, depending on the study. This can be related to different morphology [54] and nanostructured layer thickness [26].

Based on previous reports [11], nanoplate WO₃ [51], 3D inverse opals WO₃ [55], and nanosponge WO₃ [56] had a higher photocurrent density of 3.7 mA cm⁻² at 1.23 V vs. RHE, ≈4 mA cm⁻² at 1.5 V vs. SCE (saturated calomel electrode), and 3.04 mA cm⁻² at 1.5 V vs. RHE, respectively. Respinis et al. reported that helium-induced nanostructured WO₃ annealed using the two-step procedure at 550, while 450 °C showed a photocurrent value of 0.8 mA cm⁻² at 1.23 V vs. RHE. The highest photocurrent density in this study is 3.5 mA cm⁻² at 1.23 V vs. RHE, which is four times higher than in Respinis's

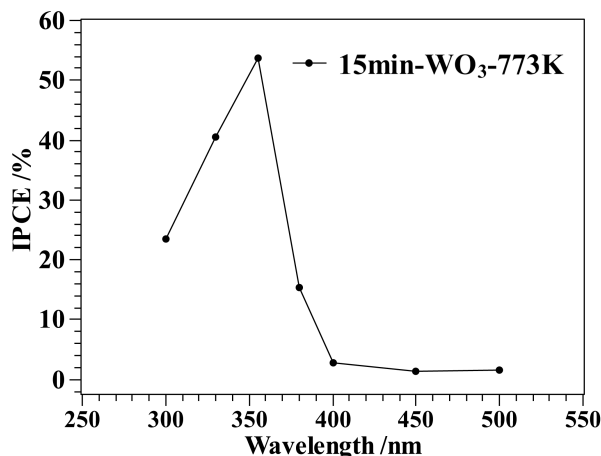


Fig. 9 IPCE measurements of the 15min-WO₃-773K.

study. This might be related to the two-step annealing process related to too thick WO₃. This research provides an experimental basis for the application of helium plasma irradiation.

4 Conclusion

In summary, a combination of plasma irradiation and calcination was used to prepare various nanostructured WO₃ photoelectrodes for PEC water splitting. The influence of helium plasma exposure time and calcination temperature dependence on PEC performances was investigated using a three-electrode cell. From the perspective of PEC performance, the 15min-WO₃-773K photoanode exhibited the highest photocurrent density. This nanostructured photoanode with an arborescent shape had a photocurrent density of 3.5 mA/cm² under the thermodynamic potential of water oxidation (1.23 V vs. RHE). The proper thickness was beneficial to the separation of electron-hole pairs. Subsequently, the temperature dependence was investigated by controlling the calcination temperature. Except for WO₃-873K, all other samples grow along the (002) crystal facet. The excellent PEC performance of WO₃-773K photoelectrodes came from the synergistic effect of proper oxide layer thickness and exposed crystal facets. An excessively thin oxide layer and low crystallinity led to low activity, whereas an excessively thick layer and a difference of preferential exposure of crystal facets increased the probability of photoexcited electron-hole pair recombination. It is shown that the plasma-treated surfaces increased the photocurrent significantly, suggesting that helium plasma irradiation can offer a novel synthesis route for fabricating the electrode for solar water splitting. Efforts to explore new semiconductor materials and improve the

PEC properties of known materials are still an important research direction in the field of PEC water splitting.

References

- [1] Esposito, D.; Levin, I.; Moffat, T.; Talin, A. H₂ Evolution at Si-based Metal-insulator-semiconductor Photoelectrodes Enhanced by Inversion Channel Charge Collection and H Spillover *Nature Mater.* **2013**, *12*, 562-568.
- [2] Moniz, S. J. A.; Shevlin, S. A.; Martin, D. J.; Guo, Z.; Tang, J. Visible-light Driven Heterojunction Photocatalysts for Water Splitting - A Critical Review *Energy Environ. Sci.* **2015**, *8*, 731-759.
- [3] Li, J.; Yan, M.; Zhou, X.; Huang, Z.; Xia, Z.; Chang, C.; Ma, Y.; Qu, Y. Mechanistic Insights on Ternary Ni_{2-x}Co_xP for Hydrogen Evolution and Their Hybrids with Graphene as Highly Efficient and Robust Catalysts for Overall Water Splitting *Adv. Funct. Mater.* **2016**, *26*, 6785-6796.
- [4] Maeda, K.; Domen, K. Photocatalytic Water Splitting: Recent Progress and Future Challenges *J. Phys. Chem. Lett.* **2010**, *1*, 2655-2661.
- [5] Lian, Z.; Wang, W.; Xiao, S.; Li, X.; Cui, Y.; Zhang, D.; Li, G.; Li, H. Plasmonic Silver Quantum Dots Coupled with Hierarchical TiO₂ Nanotube Arrays Photoelectrodes for Efficient Visible-light Photoelectrocatalytic Hydrogen Evolution *Sci. Rep.* **2015**, *5*, 10461.
- [6] Li, G.; Lian Z.; Li, X.; Xu, Y.; Wang, W.; Zhang, D.; Tian, F.; Li, H. Ionothermal Synthesis of Black Ti³⁺-doped Single-crystal TiO₂ as an Active Photocatalyst for Pollutant Degradation and H₂ Generation *J. Mater. Chem. A* **2015**, *3*, 3748-3756.
- [7] Hodes, G.; Cahen, A.; Manassen, J. Tungsten Trioxide as a Photoanode for a Photoelectrochemical Cell (PEC) *Nature* **1976**, *260*, 312-313.
- [8] Butler, M. A.; Nasby, R. D.; Quinn, R. K. Tungsten Trioxide as an Electrode for Photoelectrolysis of Water *Solid State Commun.* **1976**, *19*, 1011-1014.
- [9] Ng, K. H.; Minggu, L. J.; Kassim, M. B. Gallium-doped Tungsten Trioxide Thin Film Photoelectrodes for Photoelectrochemical Water Splitting *Int. J. Hydrog. Energy* **2013**, *38*, 9585-9591.
- [10] Liu, X.; Wang, F.; Wang, Q. Nanostructure-based WO₃ Photoanodes for Photoelectrochemical Water Splitting *Phys. Chem. Chem. Phys.* **2012**, *14*, 7894-7911.
- [11] Wang, Y.; Tian, W.; Chen, C.; Xu, W.; Li, L. Tungsten Trioxide Nanostructures for Photoelectrochemical Water Splitting: Material Engineering and Charge Carrier Dynamic Manipulation *Adv. Funct. Mater.* **2019**, *29*, 1809036.
- [12] Zheng, G.; Wang, J.; Liu, H.; Murugadoss, V.; Zu, G.; Che, H.; Lai, C.; Li, H.; Ding, T.; Gao, Q.; Guo, Z. Tungsten Oxide Nanostructures and Nanocomposites for Photoelectrochemical Water Splitting *Nanoscale* **2019**, *11*, 18968-18994.

- [13] Shabdan, Y.; Markhabayeva, A.; Bakranov, N.; Nuraje, N. Photoactive Tungsten-Oxide Nanomaterials for Water-Splitting Nanomaterials **2020**, 10, 1871.
- [14] Tang, R.; Zhou, S.; Zhang, Z.; Zheng, R.; Huang, J. Engineering Nanostructure-Interface of Photoanode Materials Toward Photoelectrochemical Water Oxidation *Adv. Mater.* **2021**, 33, 2005389.
- [15] Zhou, S.; Tang, R.; Zhang, L.; Yin, L. Au Nanoparticles coupled Three-dimensional Macroporous BiVO₄/SnO₂ Inverse Opal Heterostructure For Efficient Photoelectrochemical Water Splitting *Electrochim. Acta* **2017**, 248, 593.
- [16] Zhou, M.; Bao, J.; Xu, Y.; Zhang, J.; Xie, J.; Guan, M.; Wang, C.; Wen, L.; Lei, Y.; Xie, Y. Photoelectrodes Based upon Mo:BiVO₄ Inverse Opals for Photoelectrochemical Water Splitting *ACS Nano* **2014**, 8, 7088.
- [17] Tahir, M. B.; Sagir, M. Carbon Nanodots and Rare Metals (RM=La, Gd, Er) Doped Tungsten Oxide Nanostructures for Photocatalytic Dyes Degradation and Hydrogen Production *Sep. Purif. Technol.* **2019**, 209, 94-102.
- [18] Tahir, M. B.; Ali, S.; Rizwan, M. A Review on Remediation of Harmful Dyes Through Visible Light-driven WO₃ Photocatalytic Nanomaterials *Int. J. Environ. Sci. Technol.* **2019**, 16, 4975-4988.
- [19] Kajita, S.; Saeki, T.; Yoshida, N.; Ohno, N.; Iwamae, A. Nanostructured Black Metal: Novel Fabrication Method by Use of Self-Growing Helium Bubbles *Appl. Phys. Express* **2010**, 3, 085204.
- [20] Kajita, S.; Saeki, T.; Hirahata, Y.; Yajima, M.; Ohno, N.; Yoshihara, R.; Yoshida, N. Development of Nanostructured Black Metal by Self-Growing Helium Bubbles for Optical Application *Jpn. J. Appl. Phys.* **2011**, 50, 08JG01.
- [21] Yajima, M.; Hatano, Y.; Kajita, S.; Shi, J.; Hara, M.; Ohno, N. Tritium Retention in Nanostructured Tungsten with Large Effective Surface Area *J. Nucl. Mater.* **2013**, 438, S1142-S1145.
- [22] Lin, L.; Wang, Q. Microplasma: A New Generation of Technology for Functional Nanomaterial Synthesis *Plasma Chem. Plasma Process.* **2015**, 35, 925-962.
- [23] Komori, K.; Yoshida, T.; Yagi, S.; Yoshida, H.; Yajima, M.; Kajita, S.; Ohno, N. Application of Nanostructured Tungsten Fabricated by Helium Plasma Irradiation for Photoinduced Decolorization of Methylene Blue *J. Surf. Sci. Nanotech.* **2014**, 12, 343-348.
- [24] Tanyeli, I.; Marot, L.; Matgys, D.; Sanden, M. C. M. van de; Temmerman, G. De Surface Modifications Induced by High Fluxes of Low Energy Helium Ions *Sci. Rep.* **2015**, 5, 9779.
- [25] Tanyeli, I.; Marot, L.; Sanden, M. C. M. van de; Temmerman, G. De Nanostructuring of Iron Surfaces by Low-Energy Helium Ions *ACS Appl. Mater. Interfaces* **2014**, 6, 3462-3468.
- [26] Respinis, M. de; Temmerman, G. De; Tanyeli, I.; Sanden, M. C. M. van de; Doerner, R. P.; Baldwin, M. J.; Krol, R. van de Efficient Plasma Route to Nanostructure Materials: Case Study on the Use of m-WO₃

- for Solar Water Splitting ACS Appl. Mater. Interfaces **2013**, 5, 7621-7625.
- [27] Bieberle-Hütter, A.; Tanyeli, I.; Lavrijsen, R.; Koopmans, B.; Sinha, R.; Sanden, M.C.M. van de Nanostructuring of Iron Thin Films by High Flux Low Energy Helium Plasma Thin Solid Films **2017**, 631, 50-56.
- [28] Sinha, R.; Tanyeli, I.; Lavrijsen, R.; Sanden, M.C.M. van de; Bieberle-Hütter, A. The Electrochemistry of Iron Oxide Thin Films Nanostructured by High Ion Flux Plasma Exposure Electrochim. Acta **2017**, 258, 709-717.
- [29] Baldwin M. J.; Doerner, R. P. Helium Induced Nanoscopic Morphology on Tungsten under Fusion Relevant Plasma Conditions Nucl. Fusion **2008**, 48, 035001.
- [30] Kajita, S.; Yoshida, N.; Yoshihara, R.; Ohno, N.; Yamagiwa, M. TEM Observation of the Growth Process of Helium Nanobubbles on Tungsten: Nanostructure Formation Mechanism J. Nucl. Mater. **2011**, 418, 152-158.
- [31] Zhao, Y.; Balasubramanyam, S.; Sinha, R.; Lavrijsen, R.; Verheijen, M. A.; Bol, A. A.; Bieberle-Hütter, A. Physical and Chemical Defects in WO₃ Thin Films and Their Impact on Photoelectrochemical Water Splitting ACS Appl. Energy Mater. **2018**, 1, 5887-5895.
- [32] Kajita, S.; Sakaguchi, W.; Ohno, N.; Yoshida, N.; Saeki, T. Formation Process of Tungsten Nanostructure by the Exposure to Helium Plasma under Fusion Relevant Plasma Conditions Nucl. Fusion **2009**, 49, 095005.
- [33] Upadhyay, K. K.; Altomare, M.; Eugenio, S.; Schmuki, P.; Silva, T. M.; Montemor, M. F. On the Supercapacitive Behaviour of Anodic Porous WO₃-Based Negative Electrodes Electrochim. Acta **2017**, 232, 192-201.
- [34] Straumanis, M. E. Absorption Correction in Precision Determination of Lattice Parameters J. Appl. Phys. **1959**, 30, 1965-1969.
- [35] Sharma, L.; Kumar, P.; Halder, A. Phase and Vacancy Modulation in Tungsten Oxide: Electrochemical Hydrogen Evolution ChemElectroChem **2019**, 6, 3420-3428.
- [36] Sun, J.; Zhang, Z.; Gong, Y.; Wang, H.; Wang, R.; Zhao, L.; He, B. Plasma Engraved Bi_{0.1}(Ba_{0.5}Sr_{0.5})_{0.9}Co_{0.8}Fe_{0.2}O_{3-δ} Perovskite for Highly Active and Durable Oxygen Evolution Sci. Rep. **2019**, 9, 4210.
- [37] Zhu, Y.; Zhou, W.; Chen, Y.; Yu, J.; Liu, M.; Shao, Z. A High-Performance Electrocatalyst for Oxygen Evolution Reaction: LiCo_{0.8}Fe_{0.2}O₂ Adv. Mater. **2015**, 27, 7150-7155.
- [38] Liu, R.; Liang, F.; Zhou, W.; Yang, Y.; Zhu, Z. Calcium-doped Lanthanum Nickelate Layered Perovskite and Nickel Oxide Nano-hybrid for Highly Efficient Water Oxidation Nano Energy **2015**, 12, 115-122.

- [39] Sreethawong, T.; Suzuki, Y.; Yoshikawa, S. Synthesis, Characterization, and Photocatalytic Activity for Hydrogen Evolution of Nanocrystalline Mesoporous Titania Prepared by Surfactant-assisted Templating Sol-gel Process *J. Solid State Chem.* **2005**, *178*, 329-338.
- [40] Daniel, M. F.; Desbat, B.; Lassegues, J. C.; Gerand, B.; Figlarz, M. Infrared and Raman Study of WO_3 Tungsten Trioxides and $\text{WO}_3 \cdot x\text{H}_2\text{O}$ Tungsten Trioxide Hydrates *J. Solid State Chem.* **1987**, *67*, 235-247.
- [41] Cazzanelli, E.; Vinegoni, C.; Mariotto, G.; Kuzmin, A.; Purans, J. Low-Temperature Polymorphism in Tungsten Trioxide Powders and Its Dependence on Mechanical Treatments *J. Solid State Chem.* **1999**, *143*, 24-32.
- [42] Daz-Reyes, J.; Castillo-Ojeda, R.; Galvn-Arellano, M.; Zaca-Moran, O. Characterization of WO_3 Thin Films Grown on Silicon by HFMOD *Adv. Condens. Matter Phys.* **2013**, *2013*, 1-9.
- [43] Pecquenard, B.; Lecacheux, H.; Livage, J.; Julien, C. Orthorhombic WO_3 Formed via a Ti-Stabilized $\text{WO}_3 \cdot 13\text{H}_2\text{O}$ Phase *J. Solid State Chem.* **1998**, *135*, 159-168.
- [44] Ng, C.; Ng, Y. H.; Iwase, A.; Amal, R. Influence of Annealing Temperature of WO_3 in Photoelectrochemical Conversion and Energy Storage for Water Splitting *ACS Appl. Mater. Interfaces* **2013**, *5*, 5269-5275.
- [45] Momeni, M. M.; Ghayeb, Y.; Ezati, F. Investigation of the Morphology, Structural, Optical, and Photoelectrochemical Properties of $\text{WO}_3\text{-Fe}_2\text{O}_3/\text{CrTiO}_2$ Thinfilm Photoanodes for Water Splitting *Appl. Phys. A* **2020**, *126*, 1-9.
- [46] Pancielejko, A.; Rzepnikowska, M.; Zaleska-Medynska, A.; Ąuczak, J.; Mazierski, P. Enhanced Visible Light Active WO_3 Thin Films Toward Air Purification: Effect of the Synthesis Conditions *Materials* **2020**, *13*, 3506.
- [47] Gong, H.; Ma, R.; Mao, F.; Liu, K.; Cao, H.; Yan, H. Light-induced Spatial Separation of Charges toward Different Crystal Facets of Square-like WO_3 *Chem. Commun.* **2016**, *52*, 11979-11982.
- [48] Xie, S.; Han, X.; Kuang, Q.; Fu, J.; Zhang, L.; Xie, Z.; Zheng, L. Solid State Precursor Strategy for Synthesizing Hollow TiO_2 Boxes with a High Percentage of Reactive {001} Facets Exposed *Chem. Commun.* **2011**, *47*, 6722-6724.
- [49] Pearton, S. Doped Nanostructures *Nanoscale* **2010**, *2*, 1057.
- [50] Zhang, J.; Zhang, P.; Wang, T.; Gong, J. Monoclinic WO_3 Nanomultilayers with Preferentially Exposed (002) Facets for Photoelectrochemical Water Splitting *Nano Energy* **2015**, *11*, 189-195.
- [51] Wang, S.; Chen, H.; Gao, G.; Butburee, T.; Lyu, M.; Thaweesak, S.; Yun, J.; Du, A.; Liu, G.; Wang, L. *Nano Energy* **2016**, *24*, 94-102.
- [52] Xie, Y. P.; Liu, G.; Yin, L.; Cheng, H. Crystal Facet-dependent Photocatalytic Oxidation and Reduction Reactivity of Monoclinic WO_3 for Solar Energy Conversion *J. Mater. Chem.* **2012**, *22*, 6746-6751.

- [53] Liu, X.; Wang, F.; Wang, Q. Nanostructure-based WO₃ Photoanodes for Photoelectrochemical Water Splitting Phys. Chem. Chem. Phys. **2012**, 14, 7894-7911.
- [54] Li, W.; Li, J.; Wang, X.; Luo, S.; Xiao, J.; Chen, Q. Visible Light Photoelectrochemical Responsiveness of Self-organized Nanoporous WO₃ Films Electrochim. Acta **2010**, 56, 620-625.
- [55] Chen, X.; Ye, J.; Quyang, S.; Kako, T.; Li, Z.; Zou, Z. Enhanced Incident Photon-to-Electron Conversion Efficiency of Tungsten Trioxide Photoanodes Based on 3D-Photonic Crystal Design ACS Nano **2011**, 5, 4310-4318.
- [56] Nakajima, T.; Hagino, A.; Nakamura, T.; Tsuchiya, T.; Sayama, K. WO₃ Nanosponge Photoanodes with High Applied Bias Photon-to-current Efficiency for Solar Hydrogen and Peroxydisulfate Production J. Mater. Chem. A **2016**, 4, 17809-17818.